

REPORT DOCUMENTATION PAGE			Form Approved OMB NO. 0704-0188		
<p>The public reporting burden for this collection of information is estimated to average 1 hour per response, including the time for reviewing instructions, searching existing data sources, gathering and maintaining the data needed, and completing and reviewing the collection of information. Send comments regarding this burden estimate or any other aspect of this collection of information, including suggestions for reducing this burden, to Washington Headquarters Services, Directorate for Information Operations and Reports, 1215 Jefferson Davis Highway, Suite 1204, Arlington VA, 22202-4302. Respondents should be aware that notwithstanding any other provision of law, no person shall be subject to any penalty for failing to comply with a collection of information if it does not display a currently valid OMB control number.</p> <p>PLEASE DO NOT RETURN YOUR FORM TO THE ABOVE ADDRESS.</p>					
1. REPORT DATE (DD-MM-YYYY) 05-01-2010		2. REPORT TYPE Final Report		3. DATES COVERED (From - To) 15-Sep-2003 - 14-Mar-2009	
4. TITLE AND SUBTITLE Uncooled Tunable LWIR Microbolometer: Final Report			5a. CONTRACT NUMBER DAAD19-03-1-0343		
			5b. GRANT NUMBER		
			5c. PROGRAM ELEMENT NUMBER 611102		
6. AUTHORS Joseph J Talghader			5d. PROJECT NUMBER		
			5e. TASK NUMBER		
			5f. WORK UNIT NUMBER		
7. PERFORMING ORGANIZATION NAMES AND ADDRESSES University of Minnesota - Minneapolis Sponsored Projects Administration 450 McNamara Alumni Center Minneapolis, MN 55455 -2009			8. PERFORMING ORGANIZATION REPORT NUMBER		
9. SPONSORING/MONITORING AGENCY NAME(S) AND ADDRESS(ES) U.S. Army Research Office P.O. Box 12211 Research Triangle Park, NC 27709-2211			10. SPONSOR/MONITOR'S ACRONYM(S) ARO		
			11. SPONSOR/MONITOR'S REPORT NUMBER(S) 45608-EL.1		
12. DISTRIBUTION AVAILABILITY STATEMENT Approved for Public Release; Distribution Unlimited					
13. SUPPLEMENTARY NOTES The views, opinions and/or findings contained in this report are those of the author(s) and should not be construed as an official Department of the Army position, policy or decision, unless so designated by other documentation.					
14. ABSTRACT Uncooled infrared detection has given the United States military one of its most significant advantages of recent decades. However, this technology has spread to countries across the globe, and US superiority is no longer assured. However, uncooled detectors have significant potential capabilities that have been little explored. Cooled detectors completely dominate narrowband sensing applications, such as in target recognition or chemical identification. This is probably because thermal detectors have traditionally been designed to absorb across the					
15. SUBJECT TERMS microbolometer, infrared, detector, tunable					
16. SECURITY CLASSIFICATION OF:			17. LIMITATION OF ABSTRACT UU	15. NUMBER OF PAGES	19a. NAME OF RESPONSIBLE PERSON Joseph Talghader
a. REPORT UU	b. ABSTRACT UU	c. THIS PAGE UU			19b. TELEPHONE NUMBER 612-625-4524

FORWARD:

This report covers the final results of Army Research Office (ARO) program DAAD19-03-1-0343. Much of the report is a linked compilation of research papers of the completed work developed during the program, in particular references [68]-[70]. The Principal Investigator (and author) and his research group would like to thank Bill Clark of ARO, John Carrano formerly of DARPA, and Ray Balcerak formerly of DARPA for their support. Many of the topics of this program developed out of the DARPA PWASSP program, and it is pleasing to note that some of the most exciting findings discovered during this ARO program on uncooled narrowband detectors with near-cooled sensitivity are being continued under a grant from the Electro-optics Center.

STATEMENT OF PROBLEM:

Uncooled infrared detection has given the United States military one of its most significant advantages of recent decades. However, this technology has spread to countries across the globe, and US superiority is no longer assured. However, uncooled detectors have significant potential capabilities that have been little explored. Cooled detectors completely dominate narrowband sensing applications, such as in target recognition or chemical identification. This is probably because thermal detectors have traditionally been designed to absorb across the entire thermal infrared and the materials traditionally chosen to absorb do not lend themselves to spectral selectivity. In this report we describe micromachined uncooled detectors with tunable spectral characteristics across the long-wave infrared (LWIR, $\lambda \sim 8\text{-}12\mu\text{m}$) that can target these applications. We further describe related results on the actuation and tunable thermal characteristics of microbolometers. We conclude with a theoretical description of narrowband uncooled devices with detectivity that approaches that of cooled devices.

These devices could have enormous implications for both Defense and National Security. They could be placed in hand-held units, modified cell-phone cameras, rifle sights, and other small form factor devices for real-time chemical sensing and target recognition. Micro-UAVs and micro-satellites with these sensors would not be weight- or lifetime-limited by the amount of stored coolant. Every vehicle, surveillance device, or dismounted soldier might have hyperspectral target identification and chemical/IED detection capabilities. Further, the devices would be small and sensitive enough to detect fugitive emissions from covert chemical and nuclear weapons sites.

SUMMARY OF RESULTS:

A. UNCOOLED TUNABLE MICROBOLOMETER CAVITIES

Microfabricated optical cavities are used in a variety of spectrally sensitive devices in the visible, ultraviolet, and near-IR. Currently, telecommunications is probably the biggest application area, where they are used for resonant cavity-enhanced (RCE) photodetectors [1,

2], micro machined tunable detectors [3, 4], and wavelength-division multiplexing systems (WDM) [5, 6], among others. In the middle wavelength infrared (MWIR) and LWIR regions, the fabrication of Fabry-Perot filters are more complex because the optical materials must be infrared-compatible and the layer thicknesses must be larger [7-10].

Despite these successes, it is very difficult to build filters for uncooled LWIR thermal detectors, which has limited previous researchers to demonstrations of discretely tunable 2- or 3-color thermal detectors [11-13], rather than continuously tunable ones. The problem originates with the thermal isolation of the uncooled detector itself. Integrating a tunable Fabry-Perot cavity above a detector will create three air gaps, or 2 air gaps if one places the thermal detector layer inside the cavity. Multiple air gaps mean that there are multiple optical cavities, which may couple together to cause unwanted spectral artifacts and limited tuning.

To negate these problems, we present a single air-gap coupled absorption filter for thermal detectors using a micromachined weakly absorbing top mirror. Instead of filtering in transmission as a standard Fabry-Perot, these devices couple incident radiation into their own top plate, which serves as mirror, absorber, and thermistor all at once. The devices can be continuously tuned, and a tuning range from 8.7 to 11.1 μm with 0-42V of actuation voltage is demonstrated in this work. Additionally, the devices can also be actuated to a broadband mode at 45V where the resonance width is increased to 2.83 μm . This mode is used to enhance its sensitivity in presence of low-light signals with less spectral information. Experiments have shown that the devices have switching times of about 100 μsec and settling times of about 400-700 μsec , making them compatible with focal plane array frame rates.

DESIGN

The concepts in this report apply to all thermal detectors, but in this work, they are demonstrated using a microbolometer. Figure 1 shows a diagram of the microbolometer cavity. The IR absorbing material is deposited on the top of the upper plate of germanium (Ge). A thin layer of chromium (Cr) is chosen as the absorber because it is convenient for deposition and it has the most desirable optical constants of common metals. A key characteristic of Cr is that it produces a reasonably symmetric resonance with respect to wavelength. The bottom mirror is a modified quarter-wave distributed Bragg reflector (DBR), composed of Ge and zinc sulfide (ZnS) on the top of an evaporated gold/chromium (Au/Cr) reflector with reflectivity centered around 10 μm .

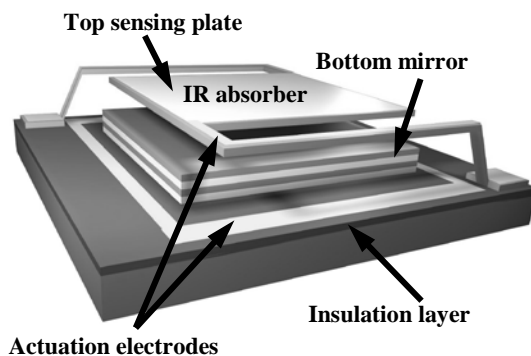


Figure 1. Conceptual diagram of a tunable absorption filter for LWIR microbolometers. The primary actuation electrodes are on the support beams and substrate to delay snap-through and enhance tuning range.

The filter works in two modes. One is broadband IR reflection/absorption detection mode that is designed to maximize the thermal light absorbed. In this mode, a 45V actuation voltage pulls the top plate near the bottom mirror, creating a very small gap ($\ll \lambda/10$). The top mirror itself does not touch the DBR mirror but instead the beam supports make contact so as not to thermally short the device. Although the contact area has not been measured in these devices yet, it is desirable to design the top movable structure such that the contact area is small enough to not affect the thermal performance [14].

The other mode is a reflection/absorption narrowband detection mode, achieved by using 0-42V actuation voltage to electronically control the air-gap over a distance of 4.3 to 6.4 μm . The position of the absorption resonance is continuously tuned, and a sharper resonance is obtained with the non-zero air gap. This mode can be used to recognize objects with subtle differences in emissivity spectrum, which are difficult to identify using standard bolometers [15]. Although this report only describes single devices, the design is compatible for use with a read-out integrated circuit (ROIC) beneath the bottom mirror, which would have the ability to control individual pixels in an array.

The top mirror is designed to have low thermal mass so that the thermal response time is small in the final detector. The resonance width (about 1.5 μm in proposed device) matches many coarse spectral features in LWIR. An optimization program based on transmission matrix simulations [16] is used to optimize the layer structure. The optimized results are listed in Table 1.

Table.1 Layer structure of the experimental devices in this study. (The optical constants of these materials have been taken from Palik [17].)

Material	Thickness	n	k
Cr	18 Å	11.8	29.8
Ge	0.6292 μm	4	0
Air gap	3.7-6.8 μm	1	0
Ge	0.1480 μm	4	0
ZnS	0.5557 μm	2.2	0
Ge	0.2456 μm	4	0
ZnS	0.5597 μm	2.2	0
Au	0.50 μm	12.24	54.7
Cr	300 Å	11.8	29.8
Si substrate	...	3.42	...

EXPERIMENTAL DETAILS

The fabrication of LWIR absorption filters differs from many micromachining processes because of the unusual IR optical materials. The fabrication procedure is illustrated in Figure 2.

First, a silicon nitride layer is deposited with low-pressure chemical vapor (LPCVD) on a four inch n-type (100) silicon wafer. To enhance the bottom mirror reflectivity, a layer of Au with a seed layer of Cr is then evaporated on the nitride open areas, followed by two Ge/ZnS quarter-wave pairs (for $\lambda \sim 10\mu\text{m}$) deposited via RF magnetron sputtering. The quarter-wave layers are patterned to form bottom mirrors. The deposition properties of the Ge and ZnS are adjusted to get consistently low-stress films and acceptably fast deposition rates. CF_4 and H_2 plasma are used to dry etch the Ge and ZnS layers respectively. After completing the substrate reflector, Au and Cr layers are deposited to form the electrode lines that surround the bottom mirrors. A sacrificial layer of SiO_2 with nominal thickness of $6.8\mu\text{m}$ is then deposited, which will later form the air gap. A polyimide sacrificial etch was originally attempted and abandoned later because it required a pure-oxygen etch-release that caused too many defects in the optical films. After patterning the anchor holes for the supports, the top-plate structural Ge layer is sputtered, followed by a thin evaporated Cr metal (patterned using lift-off) for absorption. Next, Au and Cr films are evaporated along the supporting beams and bonding pads to provide electrical contacts to the top plate for actuation. Finally, the devices are released in a diluted buffered oxide etchant and dried with a critical point dryer to prevent stiction.

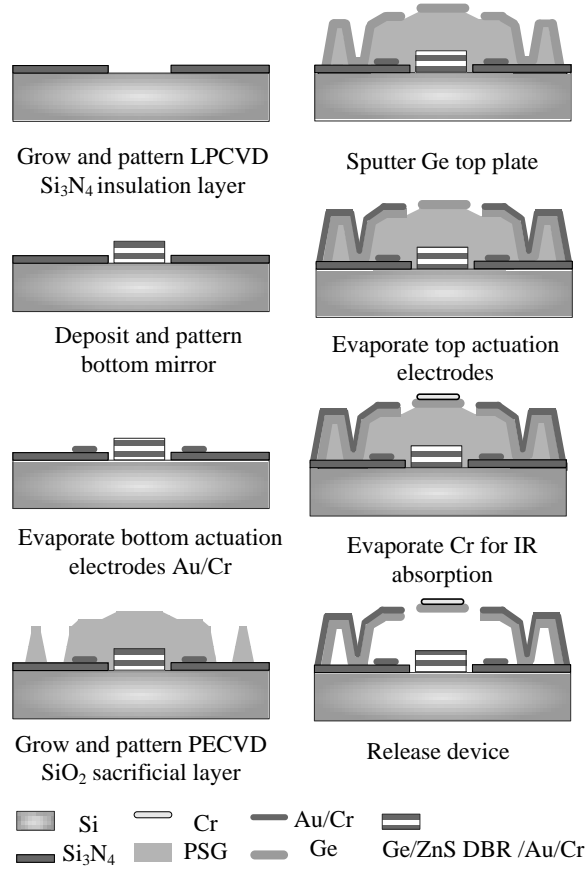


Figure2. Process flow for the LWIR wavelength tunable microbolometer filter.

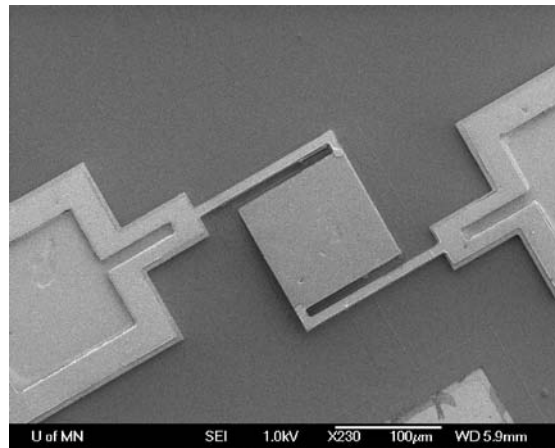


Figure 3. SEM image of a device after etch release. The top plate is 100 by 100 μm and is supported by two 150 by 5 μm beams. Au/Cr has been evaporated on the beams and anchors for actuation. The two structures to the left and right are bonding pads for later testing.

Figure 3 shows a SEM micrograph of a typical finished filter pixel. The top plate flatness deviation is less than $\lambda/16$ of the design wavelength ($\lambda \sim 10\mu\text{m}$). The temperature during fabrication (after finishing the initial silicon nitride insulation layer) does not exceed 200°C, making the process compatible with read-out integrated circuits (ROIC) beneath the bottom mirror.

MEASUREMENTS AND SIMULATION

The areas of the filters varied from $25 \times 25 \mu\text{m}^2$ to $120 \times 120 \mu\text{m}^2$. The measured resistance of the top plates is about $35 \text{K}\Omega$ at room temperature. The Cr/Ge plate has a temperature-sensitive resistance with a coefficient of approximately $0.07\%/K$.

A spectrum simulation, which incorporates the fabricated structure thickness and the mirror profile parameters measured by a Zygo interferometric microscope, has been carried out in to determine the air gap spacings that correspond to each wavelength. Figure 4 shows the evolution of the reflected peaks at different air gaps. Note that since there is no transmission, the absorption spectrum is $1-R$. Also, the simulation indicates that nearly all light absorption happens within the top Cr layer on the device, which is necessary for efficient thermal detection.

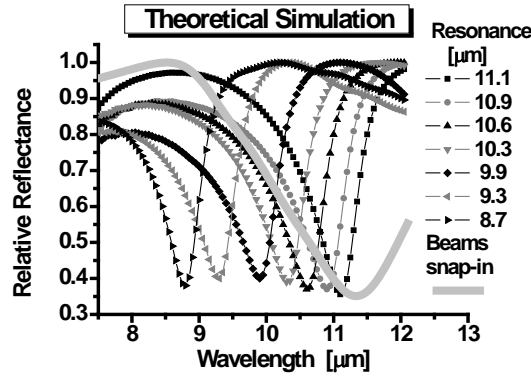


Figure 4. Spectral simulation of the experimental devices. This simulation includes the layer structure of Table 1 and a small curvature present in the top plate that broadens the resonance

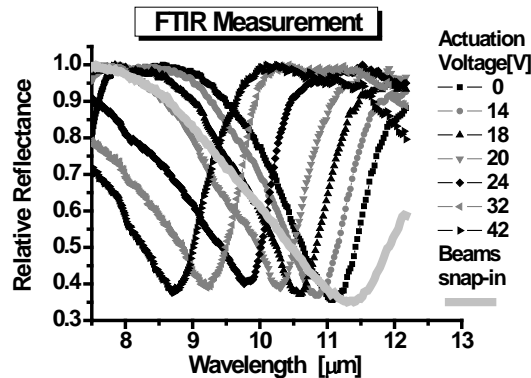


Figure 5. FTIR measurement of the relative reflectance spectra of a 120 by $120 \mu\text{m}$ square filter. As the applied voltage is varied from 0 - 42V , the narrowband resonance shifts from

11.1 μm to 8.7 μm . A broadband resonance centered at 11.3 μm is created when the voltage is increased to 45V.

The relative reflectance of the 120x120 μm^2 prototype is measured using a Nicolet Magna 750 Fourier Transform Infrared Spectroscopy (FTIR) system with microscope attachment. The filter does not transmit measurable light through the substrate. During the FTIR measurement, a voltage is applied on the supporting arms and the surrounding electrodes beneath the arms using a Keithley 230 Programmable Voltage Source. Changing the voltage level shifts the interference peak, enabling continuous tuning. The voltage-wavelength relationship is stable and shows no hysteresis.

The measured spectrum matches well with simulation and clearly illustrates that the filter has wide continuous tunability. Specifically, the devices are tunable from 8.7 to 11.1 μm using 0-42V of actuation voltage. A broadband absorption mode is reached at 45V, where the resonance full-width-at-half-maximum (FWHM) increases to 2.83 μm , compared with approximately 1.5 μm in the narrowband operation range. The switching between these two modes is emphasized in Figure 6.

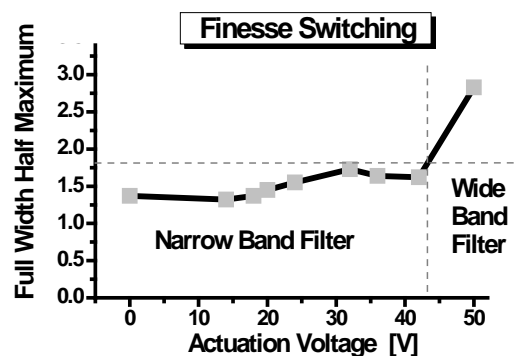


Figure 6. The resonance FWHM versus actuation voltage for the same device tested in Figure 5. The FWHM changes by approximately 87% between the tuning and broadband modes. The switch is reversible and occurs at about 45V.

To study the transient response of the filter at the onset of actuation, a position sensitive detector (PSD) is used to capture the movement of the top filter plate under a square-wave actuation voltage. The voltage pulse and the output of PSD are measured simultaneously using a digital oscilloscope. The slowest devices are those with the biggest plates, having dimensions of 120 by 120 μm . Figure 7 shows a rise time of 110 μsec with a settling time about 466 μsec , and a fall time of 96 μsec with a settling time of 672 μsec respectively. These transients are easily compatible with microbolometer thermal time constants, which are usually in the range of 5-20ms.

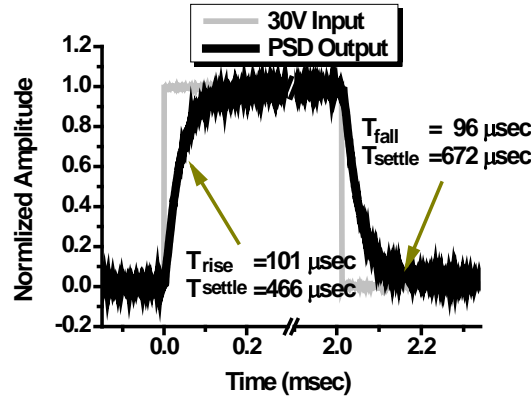


Figure 7. A typical transient response of the devices with plates of size $120 \times 120 \mu\text{m}$. The plates are supported by two beams with lateral size of $100 \times 5 \mu\text{m}$ and actuated by a 30V square wave voltage pulse.

B. MINIMUM ENERGY ACTUATION

Introduction

Many micromachined devices require surface contact and separation during operation. Typical examples include electrostatic actuated microrelays [18], RF MEMS switches [19], micromirrors in projection displays [20], and tunable thermal detectors [21, 22], *etc.* In all these devices, contact must be achieved without surface adhesion failure even after billions of cycles; therefore, control of stiction (static friction) is of critical importance.

In micro/nanoelectromechanical systems (MEMS/NEMS), various methods [23-26] have been proposed to control surface interactions during device contact operation. One widely applied technique is intentionally roughening or skewing the contact surfaces to reduce the intimate contact areas. For example, using ammonium fluoride to treat silicon surface reduces the adhesion energy at least tenfold, as the ammonium fluoride anisotropically etches the silicon surface, leaving it both rough and hydrophobic [27]. Texturing the surface with laser is commonly used in magnetic hard disk devices to create small protrusions (bumps) to alleviate the sticking forces. Bhushan and co-workers studied that the number, shape, size and pitch, etc can be further optimized to obtain lower bound for the stiction [28]. Recent work has shown that small changes to the shape of a bump from classic parabolic profile may lead to a 50% drop of the pull-off force, which is an efficient way for alleviating stiction [29]. Based on the same principle of reducing the geometrical contact area, side wall spacers [30], bumps, and stoppers are also widely used in MEMS devices. For example, Tsung-Kuan and co-workers in Intel demonstrated ULV RF switches [31] with multiple stoppers to enable zipper contact action.

An alternative approach to prevent in-use stiction failure is to increase the restoring force. One way to achieve this is through proper materials selection. For example, the Texas Instruments (TI) Digital Micro-mirror Device (DMD) uses an aluminum alloy ($\text{AlN}, \text{Al}_3\text{Ti}$ or mixture, [32]) to replace pure metal (Al) in its hinge. This change prolongs the device

operation lifetime, since in addition to an increased restoring force, it also hardens the metal (which reduces susceptibility to stiction) and minimizes creep. Another similar example is the use of gold-nickel instead of pure gold in RF switches. One may also use innovations on structural design to minimize stiction. Reference [33] uses substructure plates beneath a top plate such that the substructure provides a prying force to lift the top plate or a hammering force to store elastic energy at the contact point. Similarly the micro-mirrors in TI DMD projection systems have springs incorporated with the landing tips [32] for this purpose.

Humidity related in-use stiction failures are mainly caused by water accumulation between contacting surfaces, but it can often be avoided by packaging the MEMS device in a hermetic or inert environment. Other humidity related release-stiction failures are often solved by engineering the etch-release process or releasing devices via various drying techniques [25, 34].

Laser pulses can be used to repair structures that have failed due to stiction. Phinney and Rogers [35] demonstrated a repairing yield of 100% for cantilevers up to 1mm in length by directing a Q-switched Nd:YAG laser pulse on the backside of a device wafer. This apparently induces a thermal gradient between device and substrate which creates enough strain energy to free the stuck part. Similarly Gupta et al repaired stuck cantilevers on the wafer using laser-induced stress waves, which are introduced by directing a laser beam toward a sandwich structure composed of two transparent holding plates and the device wafer[36]. Other repair mechanisms include ultrasonic actuation and pulsed Lorentz forces.

For RF MEMS capacitive switches, dielectric charging is a primary cause of stiction failure. A bipolar actuation voltage has been used to improve the switch reliability [19]. Another solution is to use metal-dielectric-metal structural design, although this has the drawback of increasing the fabrication complexity. Alternatively one can increase the conductivity of the dielectric layer to reduce structure charging at the sacrifice of capacitance ratio.

Sandia National Laboratories [37, 38] has performed very interesting and relevant work by applying a soft-landing waveform to RF switches to achieve no-bounce actuation. The concept is that if an RF switch makes contact at zero velocity, the rebound effect commonly seen in RF switches can be minimized or eliminated. The voltage form is composed of a high level actuation pulse, then a short coast period (zero voltage level) followed by a hold voltage level. Using this method, the switches close with no rebound and obtain better electrical signal. This work is applied primarily for metal-metal contacts, but serves as the starting point for the work of this report on interface and stiction control for non-conductive contact interfaces.

All of the above techniques have their own advantages, but there are certain areas where each may have limitations. Surface roughness can only lower contact area to a certain degree. Surface coatings will affect device physical properties and lifetime, especially for thermal and optical sensors. Incorporating sophisticated mechanical designs may exceed the cost and development time for a given process. Finally, freeing the stuck devices using laser pulses may not be feasible in the field. It is highly desirable to resolve in-use stiction under normal operating conditions. Building on recent RF switching work [37, 38] to prevent rebound, we propose a minimum energy actuation scheme to minimize impact force between non-conducting interfaces. We map out device actuation regimes with stiction, without

stiction, with rebound, and without rebound and provide models for each. Extended lifetime testing of ostensibly stiction-free devices is not described as it is beyond the scope of this report and the capabilities of our multi-user laboratory. The technique allows one to separately determine actuation energy and the static pressure applied across the interface, which is extremely useful for devices where one wishes to actively control the thermal conductance [21-22]. The method uses a simple voltage waveform composed of a pull-down high level voltage pulse and a lower level hold down voltage. By adjusting the pulse length and height, one may bring the device in contact with the fixed substrate and then release it. Furthermore, the contact area and pressure of the beam and the substrate is controllable without stiction via the hold-down voltage.

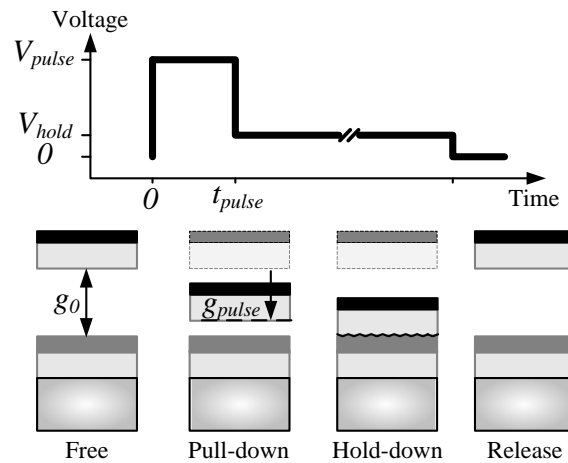
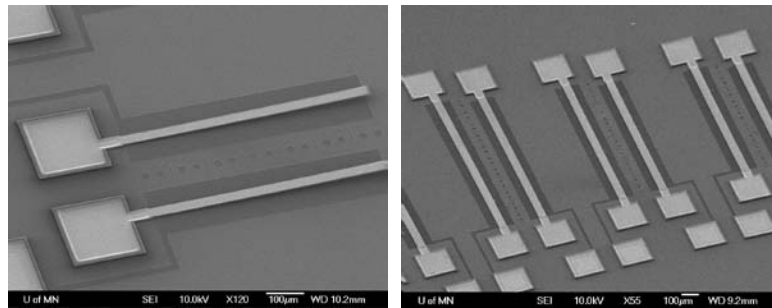
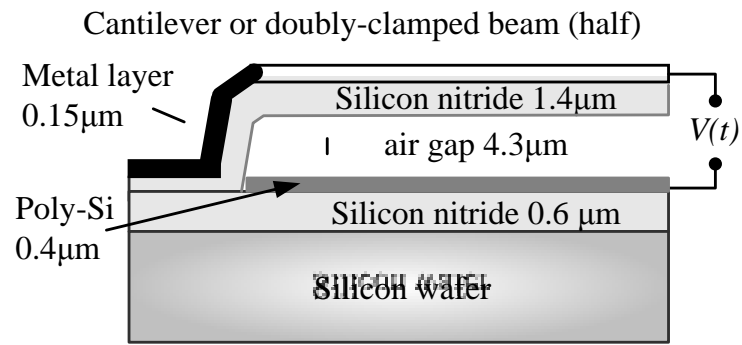


Fig.8 Schematic diagram of minimum energy actuation. (a) Conceptual diagram of the cross section view of a free cantilever or a half of a doubly-clamped microbeam. (b) SEM micrographs showing 50 μm wide beams after etch release. The displayed doubly-clamped beams have lengths ranging from 800-1000 μm and the cantilevers from 700 μm to 720 μm . The dark regions on the substrate are the bottom actuation conductors. (c) Minimum energy actuation scheme. The pull-down voltage pulse has a level of V_{pulse} , and length of t_{pulse} , the V_{hold} is the low level dc hold-down voltage. The beam releases back to the free state after the hold down voltage ceases.

The principle of the actuation, which we will call the “minimum energy” method, is to reduce the actuation energy to the minimum necessary to pull the beam in contact with the substrate. If a constant voltage is applied to a parallel-plate electrostatic actuator, a continuously increasing amount of actuation power will be transferred to the device as it approaches the substrate. Therefore the device strikes the substrate surface with great force, which is likely to damage the contacting surfaces and contribute to in-use stiction. However, if a short voltage pulse of appropriate amplitude is applied at the beginning of the actuation cycle and removed before the device crosses the pull-in instability point [39], the beam will travel gently to the substrate and touch down with minimum force. Here the term “short” means comparable to or shorter than the mechanical response time of the device. The device supports will have a restoring force that will tend to bring the device back to its equilibrium position. Since the device and substrate are essentially in contact except for a thin dielectric layer, a small hold voltage will suffice for maintaining the actuation. Conceptual diagrams of the devices and voltages used in this study are shown in Figures 8(a) and (c).

In this report we describe, model and verify the pulse energy that is necessary to achieve minimum energy actuation under a variety of voltage levels and pulse lengths. The characteristics of the hold voltage are then explored. We find that high hold voltages have little effect on device release so long as the initial pulse remains unchanged. This will be important in future applications where the heat transfer across interfaces could be changed by electrostatically applying a variable pressure. When applying an actuation pulse that is significantly longer than required for minimum energy actuation, it is found that there is a tiny time interval over which a device will pull-in and bounce back after switching to the low dc hold-down voltage level. Finally, it is observed that an ultra-short voltage pulse can repair stuck beams.

This report is organized as follows. In section II, the theory of minimum energy actuation is explained. The microbeam fabrication procedure and the experimental setup are illustrated in section III. Experimental results, simulations, and a detailed discussion of minimum energy actuation, bounce-back, and beam-release as presented in section IV. Section V provides the conclusions.

II. Background

● Actuation theory

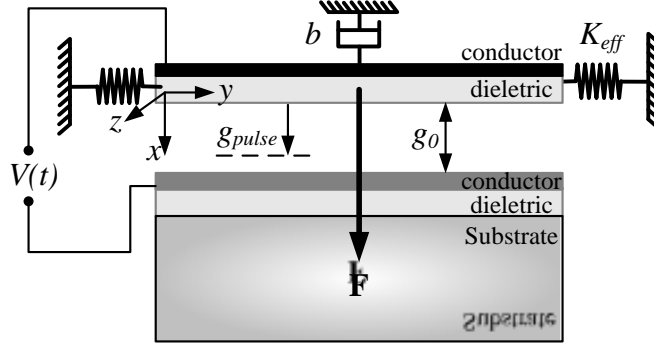


Fig.9 1-D doubly-clamped microbeam model with labels.

Consider an actuated microbeam, as shown in Figure 9, with an effective spring constant K_{eff} . This spring constant also includes a component corresponding to the beam residual stress. The total electrostatic actuation force is labeled as F , which is created by the actuation voltage $V(t)$. The air gap has the dimension of g_0 , g_{pulse} is the gap height at which the beam actuation voltage switched to the hold-down level. The squeeze film damping coefficient is labeled as b . The dielectric layer in the beam structure has the thickness of g_r and relative permittivity of ϵ_r . The beam has width of W , thickness of t and length of L . The beam area is denoted as A and the effective moving area is denoted as A_{eff} . The beam is moving in the x direction, and the lateral axis is y .

In the simplest case, considering only ideal elastic forces, the minimum energy necessary to cause the beam to reach contact is exactly equal to the potential energy stored in the beam at maximum deflection. The energy equation for the beam can be expressed as:

$$\frac{k_{eff} g_0^2}{2} = \int_0^{g_{pulse}} F(t < t_{pulse}, V = V_{pulse}) dx + \int_{g_{pulse}}^{g_0} F(t > t_{pulse}, V = V_{hold}) dx \quad (1)$$

where the left hand term is the potential energy, the first term on the right is the kinetic energy given by the initial high pull-down voltage pulse, and the second term is the kinetic energy given by the smaller hold-down voltage. Here, g_0 is the original air gap beneath the microbeam and the substrate. V_{pulse} and t_{pulse} are the pull-down voltage pulse level and length respectfully, and V_{hold} is the hold-down dc voltage level. g_{pulse} is the beam height at the time pull-down voltage pulse ceases. Thus, there is no extra kinetic energy for the beam at the time of substrate contact. The minimum energy actuation voltage waveform is listed in equation (2).

$$V(t) = \begin{cases} V_{pulse} & 0 < t < t_{pulse} \\ V_{hold} & t_{pulse} \leq t \end{cases} \quad (2)$$

For more complicated cases, the beam movement will be affected by the squeeze film damping, the large-displacement and the beam stretching effect. The dynamic simulation based on finite difference method is described in the following subsection.

● Dynamic simulation

The dynamic response of a homogeneous microbeam is given by the solution of one-dimension differential equation:

$$\begin{aligned} \frac{\partial^2}{\partial x^2} (\tilde{E}I \frac{\partial^2 w}{\partial x^2}) - \frac{b}{L} \frac{\partial w}{\partial t} + m \frac{\partial^2 w}{\partial t^2} - [\frac{\tilde{E}A}{2L} \int_0^L (\frac{\partial w}{\partial x})^2 + \sigma A] \frac{\partial^2 w}{\partial x^2} \\ = F_{electrical} + F_{VDW} \end{aligned} \quad (3)$$

where x is the position along the beam length, t is time, w is the displacement in the x direction, as shown in Fig. 9. L is the length of the beam, A is the cross-sectional area of the beam, $A=Wt$, where W is the beam width and the t is the beam thickness. The 1st term on the left side of the equation is the bending force, which is described by Bernoulli-Euler equations. Here I is the beam momentum of inertia, $I=Wt^3/12$. \tilde{E} is the effective Young's modulus of the beam material (silicon nitride) $\tilde{E}=E/(1-\nu^2)$, and ν is Possion's ratio. The 2nd term represents the squeeze-film damping; b is the damping coefficient in units of kilogram per second. The 3rd term represents inertial forces via the kinetic energy of the beam per length; m is the beam mass per unit length. The 4th term is the mid-plane stretching [40], and the last term represents the internal stress due to beam deposition conditions, where σ is the residual stress along the axial direction. This term is only included during simulations of doubly-clamped beams.

On the right side, there are two forces (per unit length). The first one is the electrostatic force,

$$F_{electrical} = \frac{\epsilon_0 W V^2(t)}{2 \left(g_0 + \frac{g_r}{\epsilon_r} - w \right)^2} \quad (4)$$

where g_0 denotes the nominal air gap between the beam and the substrate ($g_0=4.3\mu m$), and g_r and ϵ_r are the thickness of the silicon nitride structure and its relative permittivity, respectively ($g_r=1.4\mu m$, $\epsilon_r=7$). ϵ_0 is the vacuum permittivity ($\epsilon_0=8.8542 \times 10^{-12} F/M$). The instantaneous gap is g_0-w , and $V(t)$ is the applied actuation voltage. The second term on the right, F_{VDW} , represents the attractive and repulsive Van der Waals forces, following Alessandro and Paolo [41]. The contact force per unit length is expressed as equation (5), with the constants $C_1=10^{-80} Nm$ and $C_2=10^{-75} Nm$.

$$F_{VDW} = \frac{c_1 W}{(g_0 - w)^3} - \frac{c_2 W}{(g_0 - w)^{10}} \quad (5)$$

The beam equation (3) is first discretized using finite-difference (FD) methods and then converted to an ordinary differential equation (ODE), which is solved using the intrinsic ODE solver in Matlab. The boundary conditions (BC) used for discretization are listed in equation (6). For doubly-clamped beams, the BC assumes half-beam symmetry as shown in equation (7).

$$w(0)=0, \quad \frac{\partial w(0)}{\partial x}=0, \quad \frac{\partial^2 w(L)}{\partial x^2}=0, \quad \tilde{E}I \frac{\partial^3 w(L)}{\partial x^3}=0 \quad (6)$$

$$w(0)=0, \quad \frac{\partial w(0)}{\partial x}=0, \quad \frac{\partial^2 w(L/2)}{\partial x^2}=0, \quad \tilde{E}I \frac{\partial^3 w(L/2)}{\partial x^3}=0 \quad (7)$$

When considering the van der Waals contacting force, a 2nm r.m.s. surface roughness is included in the simulation to avoid singularity problems encountered in the simulation if one

forces the model to apply to zero gap. Using dc voltage actuation, the final beam center (of the doubly clamped beams) equilibrium spacing is around 10nm, rather than contact, which is consistent with the result from [42-44].

The damping factor of the air layer underneath the microbeams is dominated by the squeeze film damping effect. To simulate this, a quality factor Q needs to be calculated first, as shown in equation (8) for a doubly-clamped beam. This equation also includes a large-displacement-component [19]:

$$Q = \frac{\sqrt{E\rho}t^2}{\mu_{eff}(WL/2)^2} g_0^3 \cdot (1.1 - \left(\frac{w(x)}{g_0}\right)^2)^{3/2} \quad (8)$$

where ρ is the density of beam material. μ_{eff} is the effective gas viscosity considering the slip boundary condition, which is given by

$$\mu_{eff} = \frac{\mu_0}{1 + 9.638K_n^{1.159}} \quad (9)$$

where the Knudsen number K_n is the ratio between the molecular mean free path in air under one atmosphere (the condition under which we performed our testing) and the gap distance.

Finally the damping coefficient is given by $b = \frac{\sqrt{km}}{Q_{eff}}$, where k is the effective spring

constant [44]. (In our simulations, the damping coefficient calculated using this method is too high to match our experimental re-bounce results. Similar observations can also be found in [45].) If the squeeze film damping is significantly decreased or neglected, the beam will have bounce phenomena upon closure, as described later. Increasing b delays the beam's first closure time, but with less bouncing. The parameters used in the simulation are summarized in Table 2.

Table 2. The geometrical size and material parameters used in simulation

Doubly-clamped beam length	$L=800 \mu\text{m}$
Doubly-clamped beam width	$W=50 \mu\text{m}$
Silicon nitride beam thickness	$t=1.4 \mu\text{m}$
Air Gap	$g_0=4.3 \mu\text{m}$
Young's modulus for Silicon nitride	$E=290 \text{ GPa}$
Poisson ratio for silicon nitride	$\nu=0.28$
Silicon nitride permittivity	$\epsilon_r=7$
Silicon nitride density	$\rho=2843 \text{ Kg/m}^3$
Mean free path	$\lambda=65 \text{ nm}$
Attractive constant	$C_1=10^{-20} \text{ Nm}$
Repulsive constant	$C_2=10^{-75} \text{ Nm}^8$
Surface roughness	20 \AA

III. Processing procedure and experiment setup

The fabrication procedure of both the cantilevers and doubly-clamped microbeams begins with the deposition of a 6000 \AA insulation layer of low pressure chemical vapor deposited

(LPCVD) silicon nitride on both sides of a 4" silicon wafer. This is followed by a 4000 Å phosphine-doped LPCVD polysilicon conducting layer that is patterned to form the fixed substrate conductors. A 4 µm layer of LPCVD phosphosilicate glass (PSG) is then deposited and patterned as the sacrificial layer. A 1.4 µm LPCVD low stress silicon nitride layer is then deposited and patterned to form the beam structure layer. A chromium/gold (Cr/Au) metallization is deposited on top of the beams to form electrical contacts. A buffered hydrogen fluoride (BHF) etch is used to release the microbeams, and this is followed by Critical Point Drying (CPD).

SEM photos of the finished devices are shown in Fig. 8(b). The fabricated beams have lengths ranging from 100µm to 1200µm, and widths of 10µm, 30µm and 50µm. A grid scale is etched into the substrate between pairs of beams for easy length measurement during testing. Each beam has two conducting pads on each end and one conducting pad for the substrate counter-electrode. The solid contact interface is formed by the silicon nitride beam and the polysilicon layer.

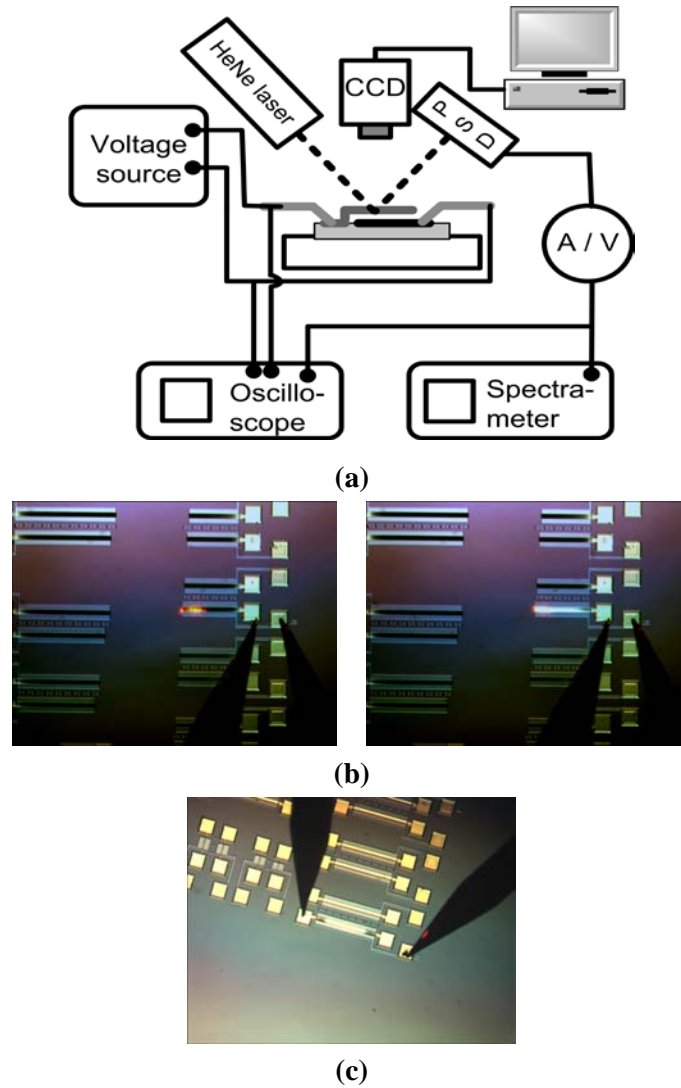
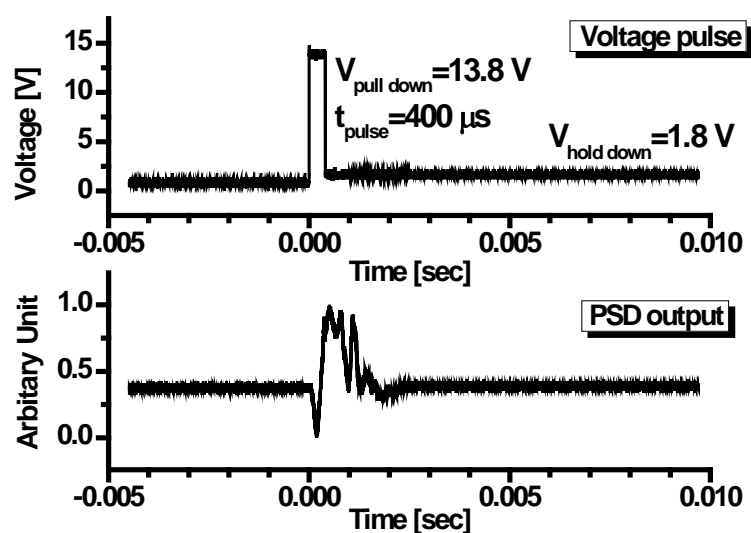


Fig. 10 The experimental setup. (a) Schematic drawing: A HeNe laser beam shines on the microbeam surface, and the reflected light is captured by a position sensitive detector (PSD). The mechanical beam spectrum is collected with a digital oscilloscope and spectrum analyzer. (b) SEM photos of cantilevers during testing. The left photo shows an unactuated

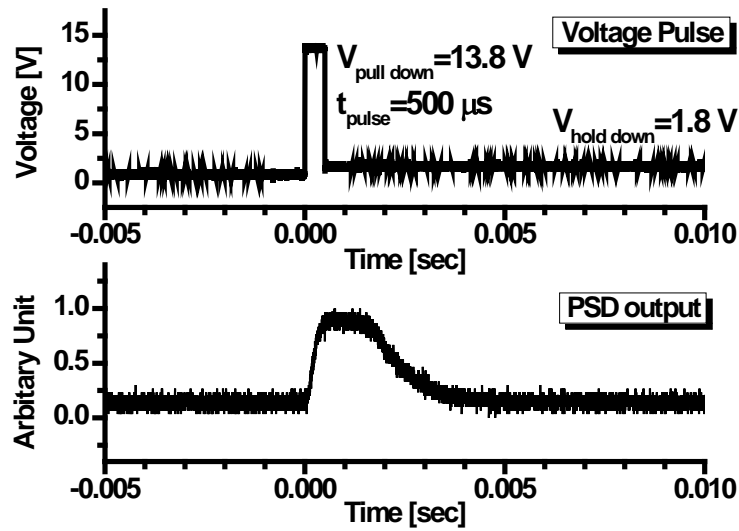
beam while the right shows one at snap down. The red spot is the laser. Two micro-probes applied the voltage $V(t)$ on the pad. After releasing the hold-down voltage, the beam springs back to its equilibrium position.

The position of the beam during testing is determined using an optical lever experiment at room temperature in a standard lab atmosphere, as illustrated in Fig. 10. A HeNe laser shines on the microbeam surface, and the reflected light is monitored by a position sensitive detector (PSD). The laser spot is placed on the tip of the cantilevers or the middle-point of the doubly-clamped microbeams. During actuation, a positive voltage pulse is applied to the polysilicon bottom electrodes with the released beam grounded. The movement of the beam induces changes in the PSD output and these are captured with a digital oscilloscope and spectrum analyzer, as well as recorded by a CCD camera. The measurements are repeated more than three times on different beams of similar size and shape to get an average reading. The testing of a cantilever beam during actuation is shown in Fig. 10b. An image of a doubly-clamped beam is also shown.

IV. Experimental and simulation results



(a) A voltage pulse that toggles beam without snap down



(b) Minimum energy snap-down

Fig. 11 Actuation voltage pulse and PSD output signals for an actuation cycle that: a) toggles the beam without snapping it down, and b) snaps down the beam without stiction upon release, i.e. “minimum energy” actuation. The only difference in the pulses is the duration.

Fig. 11 compares the response of cantilevers of length 600μm, width 50μm and thickness 1.4μm under short pulse actuation. Note that the same actuation voltage level can lead to different behavior in the microbeam depending on the length of the actuation pulse. The reverse is true as well. For example, if the beams are actuated with 13.5V, the beam does not snap-down to the substrate. If the beams are actuated with 13.6V, the beam snaps-down, but is easily released (repeatedly). If the beams are actuated with 14.0V, the beams snap-down and will not release due to stiction.

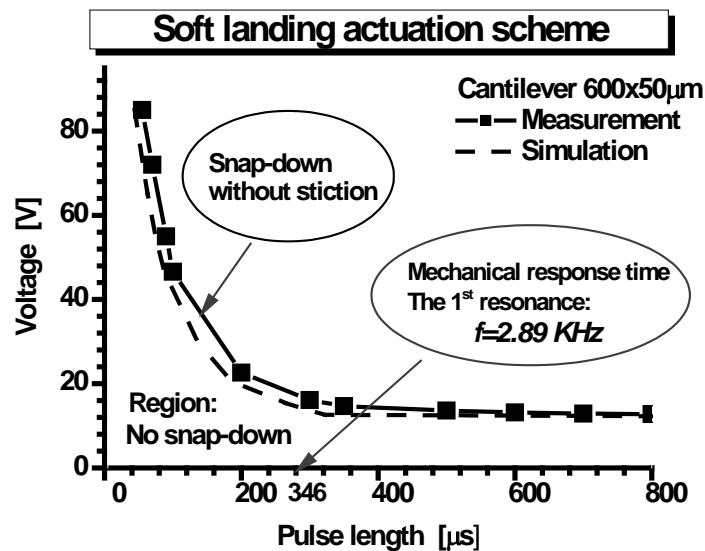


Fig. 12 Cantilevers: the minimum voltage pulse to pull-in a cantilever, which has a length of $600\mu\text{m}$ and a width of $50\mu\text{m}$. The 1st resonant frequency was measured to be 2.89 kHz. Devices actuated with this minimum energy have never shown stiction during actuation. However, the region over which stiction-free actuation occurs is extremely narrow. A few tenths of a volt higher or a few microseconds longer pulse beyond minimum snap-down will cause the beam to stick.. The hold-down voltage level is 1.8 V.

The data points in Figure 12 show the minimum voltage level and pulse duration of an actuation pulse that is needed to snap a cantilever beam down to the substrate. The gray solid line shows simulated data using the previously described model. The needed voltage level to achieve snap-down increases dramatically as the pulse width decreases. It is interesting and somewhat intuitive that the pulse width where the curve transitions from rapid changes in voltage to nearly constant voltage is around the mechanical response time of the beam. (The beam in this experiment has a mechanical response time of $346\mu\text{sec}$ as measured by scanning a sinusoidal voltage in frequency and mapping the peak of the second order filter response. The calculated results are very close the measured data. Note that the plotted minimum actuation pulse also provides release without stiction. The window for stiction-free actuation is very narrow. If the actuation pulse is applied with voltages or durations longer than shown, release may not occur. Even a 0.2V increase of the pulse amplitude or a few microseconds longer pulse duration beyond minimum can cause stiction.

The hold-down voltage level in Fig. 12 is 1.8V, but it can be increased to 4V without any noticeable release problems. It also adds a very small amount of energy to the actuation. The higher the hold level, the shorter the pull-down pulse length needs to be. For example, the 1.8V level works for an initial pulse of 12.8V. Different hold-down voltage levels will change the contact area between the beam and the substrate, and by extension, the thermal contact conductance of the device/substrate interface.

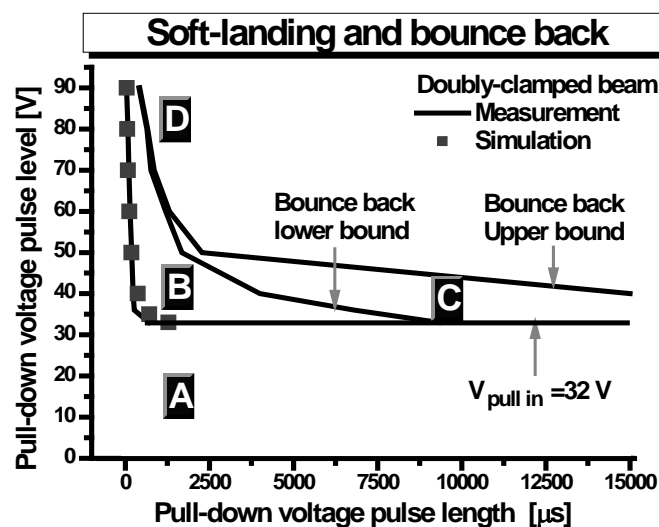
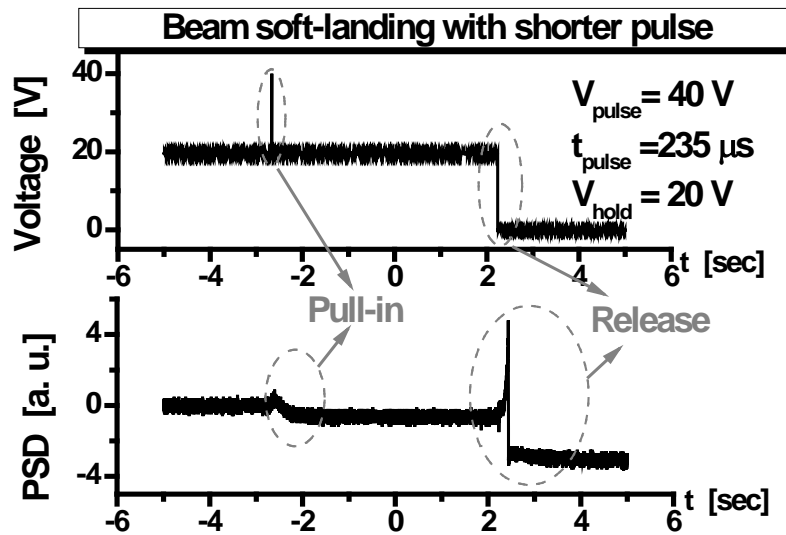


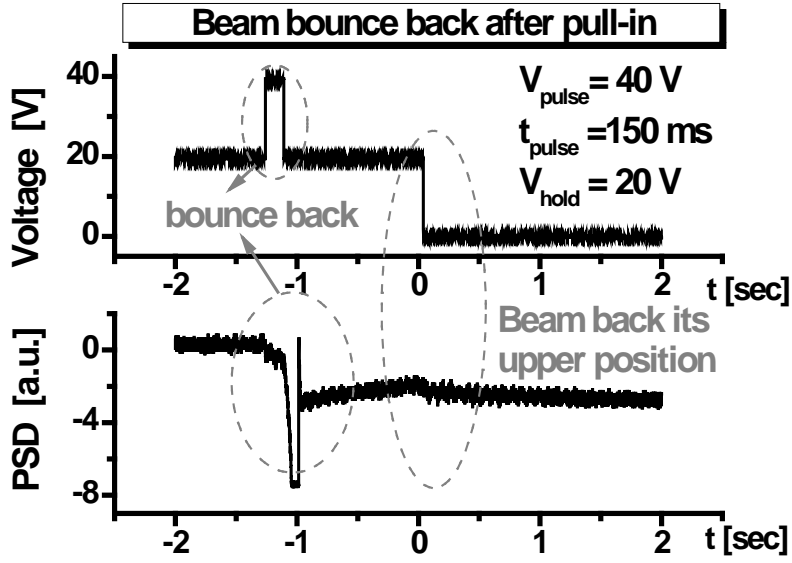
Fig. 13 Actuation behavior of a doubly-clamped beam. The beam whose measured data is shown had a length of $800\mu\text{m}$ and a width of $50\mu\text{m}$. Five different regions of behavior were

observed. The actuation of the doubly-clamped beam can be divided into several regions: actuation without snap-down (region A), snap-down without stiction (region B), snap-down with bounce-back (region C), and snap-down with stiction (region D). The simulation data is showed for the minimum energy lower limit line.

Similar experimental results for doubly-clamped beams (length $800\mu\text{m}$, width $50\mu\text{m}$ and thickness $1.4\mu\text{m}$) were performed. Fig. 13 is a map of the behavior for the clamped beams under a variety of initial pulse actuation voltages and durations. The hold voltage was kept at a constant 20V in all tests. Very short initial voltage pulses or those with low amplitude cannot snap down the beam (region A above). For slightly larger amplitudes or longer pulses, the beam will snap-down but release easily. This “minimum energy actuation” range is represented by Region B. For a given pulse level, the pulse length has a range over which the beam can be actuated without stiction. After this range, there exists a small range C where the actuation pulse will pull-down the beam then bounce it back. In region D, longer pulses cause the beam to pull-down with stiction, which cannot be released after removing the hold-down voltage.



(a)



(b)

Fig. 14 The actuation voltage and PSD signal during a “minimum energy” actuation (a) and a bounce-back actuation (b). This is the same beam measured in Fig. 13. In (a) the beam is pulled-in with $235\mu\text{s}$ voltage pulse and the PSD signal reflects the beam position change after the hold voltage is removed. In (b) the beam snaps down then bounces back with a 40V, 150ms actuation pulse. The PSD signal reflects snap-down, bounce-back, and the “toggling” of the upright beam when the hold voltage is removed.

Examples of the voltages and PSD waveforms during transitions in ranges B and C are shown in Fig. 14. In region B, the devices actuate and release when the hold voltage is removed. One can note this behavior in the rapid change of the PSD signal as the hold is released. Higher voltages or longer pulse durations cause the beam to actuate but bounce back from the substrate to nearly its equilibrium position (region C above). (The beam is lowered slightly from equilibrium due to the 20V hold voltage.) Note that the exact extent of region C varies slightly from test to test on the same device. Region C has an extent of only a few microseconds at high voltages but of milliseconds near the DC snap-down voltage. An example of the applied voltage and PSD signal for bounce-back actuation is shown in Fig. 14b. At the highest voltages and pulse durations, corresponding to region D, the beam snaps-down and sticks even after the hold voltage is released, similar to the behavior seen in region B.

Our simulations accurately predict the voltages and timings of the initial snap-down region (*the numerical values of the parameters in simulation model see table 2*). We have further tried to simulate the bounce-back phenomenon. It appears that simulations using the common expression for squeeze film damping [19] do not show a bounce back phenomenon. If we arbitrarily reduce the damping parameter by a factor of 100, the simulations *do* predict bounce back for our beams as shown in Fig. 15 but at pulse durations too short to match our experiments. This issue remains unsolved but may imply that the simplified damping value is

overestimating the results. This might take the form of a damping parameter from the numeric solution based on the Reynolds equation [29].

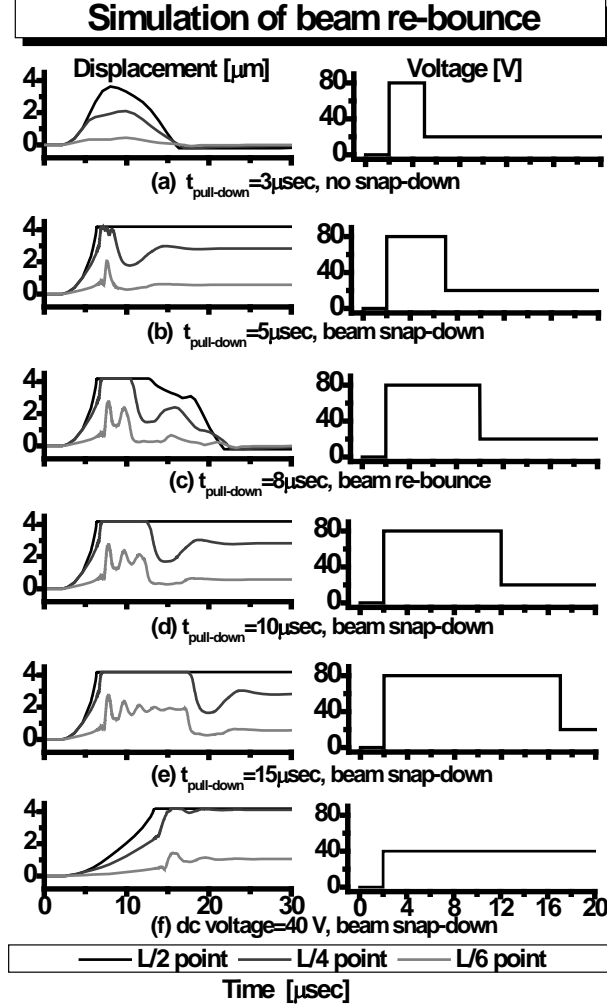


Fig. 15 - Simulation of beam displacement vs. time (left column) and actuation voltage vs. time (right column). The materials parameters used are a density of 3200 Kg/m^3 , an isotropic Young's modulus of 270 GPa , and an isotropic Poisson ratio of 0.27 . The simulation includes squeeze film damping and a van der Waals force. In part (a) the actuation toggles the beam without snap-down (range A in fig.13). In part (b) we see the minimum energy actuation range (range B in fig.13). Part (c) is the bounce back region (range C in fig.13). Parts (d) and (e) are the snap-down with stiction region (range D in fig.13). Part (f) is a simple dc pull-in actuation. Displacement curves are shown for 3 points on the doubly-clamped beam: the middle point (L/2 point), the quarter point (L/4 point) and the L/6 point.

C. THERMAL DETECTION BEYOND THE BLACKBODY NOISE LIMIT

Abstract—A generalized emissivity theory on the photon fluctuation noise of thermal detectors is presented which shows that background noise can be reduced far below that accepted by current theory. It predicts a class of narrowband detectors whose detectivity is

enhanced, counter-intuitively, by reducing the absorption of the detector across all wavelengths. This lowers the fluctuation noise, and the signal is maintained in one spectral band and direction by coupling the detector inside an $m\lambda/2$ optical cavity. In concurrence with photon detector theory, the treatment also predicts that high detectivity may be achieved by using materials with minimal absorption in the primary thermal emission bands.

The fundamental upper limit of sensitivity of a radiation detector is determined by the statistical fluctuations in the radiation exchange between the detector and its surroundings [47], [48], [49], [50]. A detector operating at this upper limit is said to be background-limited. Background-limited performance has traditionally been achieved by cooling below room temperature. This principle works for both thermal and photon detectors, but it has been particularly critical to the development of infrared photon detectors, whose operation is otherwise impacted by the thermal generation of electron hole pairs. Once thermal generation and other noise sources have been suppressed, however, the detectivity [51] is primarily governed by the overlap of background thermal emission with the spectral response of the photon detector [52]. This has not been the case for thermal detectors [53], [54].

Since the advent of modern detector theory in the 1940's, the fundamental theory of thermal detectors has been developed assuming structures with a spectrally uniform high absorption. Cryogenically cooled thermal detectors [55], [56], [57], like their photon detector counterparts, are often used with external cooled filters and shielding to eliminate unwanted background noise, but the spectral dependence of the detector itself is neglected [58]. From the point-of-view of the received signal this seems perfectly understandable since a uniform high absorption guarantees maximum light collection, but it also causes the detector to incur maximum photon fluctuation noise even when the desired signal is limited in spectral width or lies in a spectral region far from the maximum emission of the background.

One can develop a more general theory of the background fluctuation limit by realizing that the emissivity of a thermal detector may vary with direction and wavelength. We find that this is a critically important expansion of current understanding. With it, the background fluctuation noise can approach that of spectrally-selective cooled detectors and, therefore, that detectivities previously only reached with cryogenic cooling can now be attained with uncooled detectors. We predict the existence of a class of narrowband thermal detectors whose performance, counter-intuitively, increases as the absorption of the detector is reduced toward zero. We also predict that, as with cryogenically-cooled photon detectors [59] thermal detectors using materials with spectrally selective absorption will have detectivities that increase above the blackbody limit as the spectral response moves away from the peak of the background thermal emission.

A thermal detector heats in response to power absorbed from incident radiation. The lowest possible noise is caused by the fluctuations in the exchange of photons between the detector and the background. Assuming that photons obey Bose-Einstein statistics, the mean square

power fluctuation per unit detection bandwidth due to photon noise for an absorbing body at temperature T can be written as [58],

$$p_p^2 = \int_{\nu} 2h^2\nu^2 \cdot \langle(\Delta n)^2\rangle \cdot 2N \cdot d\nu$$

Assuming a Planck distribution, a Lambertian absorber and including polar and azimuthal angles, we get

$$\overline{p_p^2} = 4h^2c^3A \int_{\lambda} \int_{\theta} \int_{\phi} \frac{\epsilon(\lambda, \theta, \phi)e^{hc/\lambda kT}}{\lambda^6 [e^{hc/\lambda kT} - 1]^2} \cos \theta \sin \theta d\theta d\phi d\lambda$$

If a thermal detector had an emission below that of a blackbody (emissivity, $\epsilon < 1$), it is immediately apparent from the equation that the noise power due to background fluctuations would be reduced. Since the signal absorption decreases with the reduced emissivity, the overall signal to noise ratio also goes down. However, much as with photon detectors, if the desired signal lies within a specific spectral band, then absorption in other regions of the spectrum merely adds noise. One can adjust the absorption/emissivity to be very high in the region of the desired signal but low or zero outside it.

To date, thermal detectors have not taken advantage of this phenomenon. Many existing bolometers use interference structures [61] to enhance absorption in the LWIR so that the bolometer structure can be thinned to reduce the time constant. However these structures have been used to maximum absorption and signal in the thermal emission band rather than selectively reduce it to eliminate unwanted noise. We predict there are at least two classes of thermal detectors that could. The first is a narrowband device as shown in Figure 16. It consists of a low emissivity absorber coupled to the resonance of the optical cavity formed by two mirrors. It achieves enhanced performance by reducing the absorption of a thermal detector to very low values, reducing the background interactions. The signal is retained without loss by coupling the low absorption structure inside an optical cavity. The coupling enhances the emissivity in only one direction, which is the axis of the optical cavity, and one wavelength band, which is the resonance of the cavity. The second class of thermal detector utilizes materials whose absorption is spectrally dependent, such as a semiconductor, such that only radiation below a certain wavelength is absorbed. All the photon noise at wavelengths longer than the absorption cutoff will then be rejected. These two types of detectors will be examined in regard to the power fluctuations in turn.

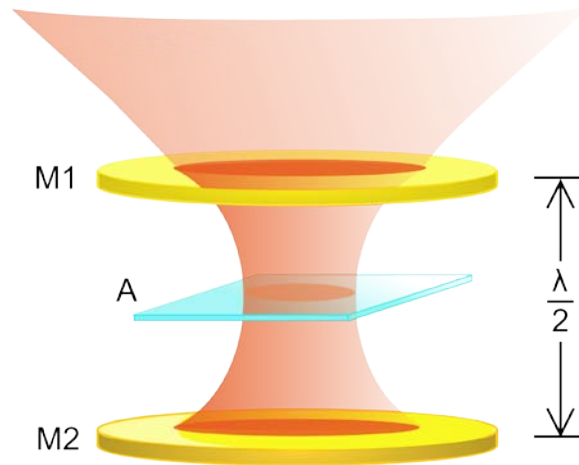


Figure 16 - Schematic drawing of a low emissivity absorber A coupled to the resonance of a cavity formed by mirrors M1 and M2.

A low emissivity detector with high coupling in one direction will have an emissivity that can be approximated by the cavity-coupled absorption within the acceptance angle of the cavity and by the detector emissivity outside this acceptance angle. This approximation becomes better as the finesse of the cavity becomes large and assumes that the Fresnel number of the cavity is high enough that diffraction losses are minimal. It also assumes that the diameter of the cavity mirrors is not so large that the acceptance angle for light in the cavity extends outside the spectral resonance.

The background fluctuations have traditionally been assumed to originate with a thermal detector with high absorption that is independent of frequency and direction. Using this assumption we can obtain a detectivity value of $1.97 \times 10^{10} \text{ cmHz}^{1/2}/\text{W}$ at room temperature and a 2π field of view. For several decades, this value has been quoted as the highest detectivity achievable at room temperature.

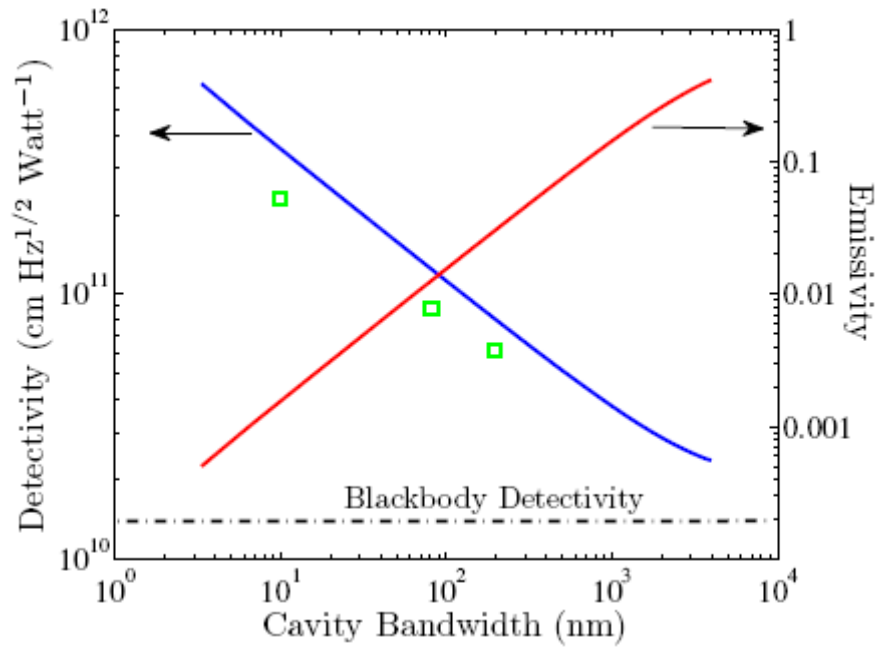


Figure 17 - A plot of room temperature photon noise limited detectivity vs. the cavity bandwidth is shown by the solid blue line. The dashed line indicates room temperature photon noise limited detectivity of a blackbody absorber with a 4π field of view. The red solid line indicates emissivity of the absorber membrane on the right axis. The green squares indicate photon noise limited detectivities of practical cavity designs an example of which is shown in Table 3.

However, if the emissivity is restricted to high values only within a narrow spectral band using a cavity coupled absorber structure, higher detectivity values can be achieved. To model this, a simple resonant cavity coupled absorber structure has been constructed from two ideal mirrors and a detector with a spectrally uniform low emissivity. For such a system the net cavity emissivity can be easily calculated analytically[62] which can then be used with the above equations to find the noise power. A plot of detectivity versus cavity bandwidth (or spectral resolution) for a cavity coupled structure is shown in Figure 17. It can be seen that the calculated detectivities are much higher than the blackbody photon noise limit. It can also be seen that the detectivity of these devices increases as the spectral resolution and field of view is narrowed. As a practical note, the reduced noise power for smaller fields on view is a significant advantage over current thermal detectors, whose low detectivities generally only make them compatible with detection at short range.

Note that the photon noise is dominated by the emissivity of the detector and radiation fluctuations away from the optical cavity axis rather than by fluctuations occurring on the resonance of the cavity itself. However, since the width of the spectral resonance determines the required emissivity for proper coupling, the detectivity increases with spectral resolution.

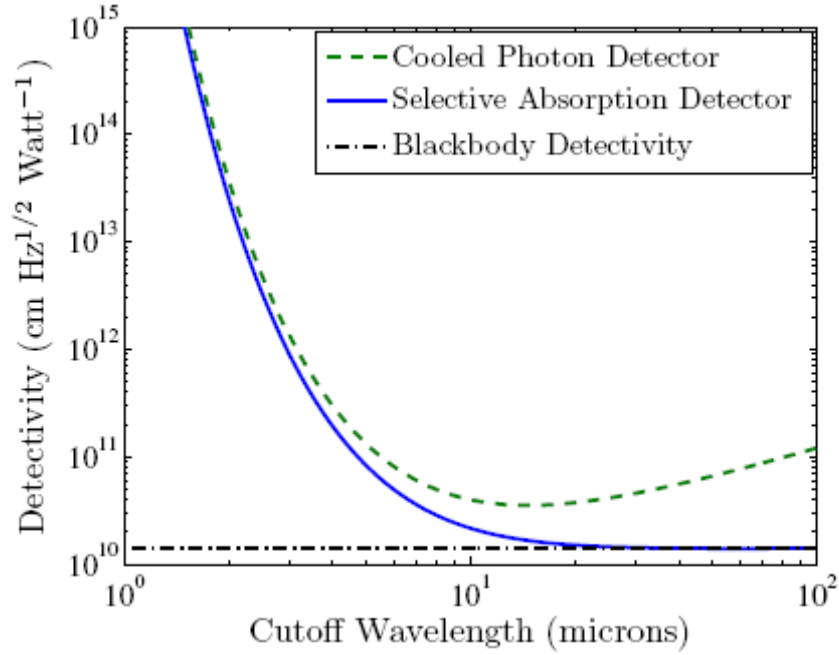


Figure 18 - A plot of photon noise-limited detectivity vs. absorber cutoff wavelength for spectrally selective thermal detector and a conventional cooled photon detector.

Figure 18 shows the variation in specific detectivity with cutoff wavelength of a background limited thermal detector having spectrally selective absorption. The absorption of the detector is assumed to be a step function with full absorption below the cutoff wavelength and zero beyond it. This is a simplified model of the spectral characteristics of semiconductors, which only absorb photons with energies below the bandgap. As the cutoff wavelength increases, the detector sees more of the 290 K background fluctuation noise and the detectivity drops. At sufficiently high cutoff wavelengths the detectivity approaches that of a spectrally broad thermal detector. This behavior is analogous to a broadband bolometer whose spectral response is limited by cooled filters[63]. In our case, this spectral limiting is achieved by using an appropriate absorber material as the thermal detector itself. The material does not need to have high crystal quality because non-radiative recombination of carriers is not critically important for this device. Also shown for comparison is the variation of detectivity with cutoff wavelength for a conventional cooled photon detector. Since photon detectors respond to the number fluctuations in photons rather than power fluctuations, this detectivity is close to that of the thermal detector at lower cutoff wavelengths but diverges at higher wavelengths.

Perhaps the most widespread thermal detector today is the bolometer. As a case study we will first discuss the construction of cavity coupled and selective absorption bolometers and then examine how they would perform in the real world in the presence of other noise sources[60]. Practical bolometer structures can be fabricated by thin film deposition and etching techniques. Two possible thin film layer structures are shown in Table 3. The narrowband bolometer is constructed from a low-emissivity doped Germanium absorber suspended between two Distributed Bragg Reflectors (DBRs). The Bragg reflectors consist of

alternating layers of Germanium and Strontium Fluoride. The free carrier infrared absorption in doped Germanium has a λ^2 dependence and can be tailored according to our requirements by changing the doping [64]. Similarly, the selective absorption bolometer is constructed from a Lead Selenide absorber suspended over a high reflectivity DBR to form an optical cavity. PbSe has an absorption cutoff at 5 μm and the cavity coupling is designed to improve its absorption in the 3-5 μm region.

Table 3 - The first section shows the layer structure for narrowband and selective absorption bolometers. The second section shows the calculated noise values. The values for the materials properties were taken from [65,66,67].

	Narrowband Detector ^a		Spectrally selective Detector ^b	
	Material	Thickness (nm)	Material	Thickness (nm)
Top Mirror	Ge	625	None	
	SrF ₂	1,811		
	Ge	625		
Spacing	Air	1,750		
Absorber	doped Ge	50	PbSe	45
Spacing	Air	2,500	Air	500
Bottom Mirror	Ge	625	Ge	250
	SrF ₂	1,811	SrF ₂	707
	3 similar Ge/SrF ₂ pairs		3 similar Ge/SrF ₂ pairs	
NEP conductance (Watt)	4.49×10^{-13}		4.48×10^{-13}	
NEP Johnson (Watt) ^c	3.67×10^{-13}		3.40×10^{-13}	
NEP 1/f (Watt) ^c	1.60×10^{-13}		1.38×10^{-13}	
Detectivity (cm Hz ^{1/2} W ⁻¹)	2.51×10^{10}		2.44×10^{10}	

^aThermal conductance $1.22 \times 10^{-8} \text{W/K}$, heat capacity $8.51 \times 10^{-10} \text{J/K}$, thermal bandwidth = 2.28 Hz

^bThermal conductance $1.05 \times 10^{-8} \text{W/K}$, heat capacity $6.39 \times 10^{-10} \text{J/K}$, thermal bandwidth = 2.62 Hz

^cNominal resistance 100 k Ω , Temperature coefficient of resistance 0.02 per K, Bias voltage 0.1 V, 1/f noise parameter $k_m = 10^{-13}$

If the detectors were purely photon noise-limited the achievable detectivities would be comparable to that of the ideal detector discussed in the previous section. This is shown in Figure 17 in which the three square data points are the photon noise limited detectivities of three different narrowband detector configurations, one of which is described in Table 3. The absorption of the layered cavity structures was calculated using the conventional matrix method [62] and then used in the fluctuation equation to calculate the detectivities. Similar to the ideal case, the mirror size is restricted so that only the resonance centered on the cavity axis is allowed. It can be seen that the photon noise-limited detectivities of these narrowband devices follow the same envelope as the ideal detector and are much higher than the blackbody photon noise limit.

In presence of other noise sources the detectivity will be reduced from the purely photon noise limited case. For single pixel bolometers, the primary noise sources are Johnson noise, 1/f noise, and thermal conductance noise. The net noise equivalent power (NEP) in presence of these noise sources is given by

$$(NEP)^2 = G^2 \frac{kT^2}{C} + \frac{1}{\mathcal{R}^2} \left(4kTR\Delta f + V_b^2 k_m \ln \frac{f_2}{f_1} \right)$$

The first term in this equation is the thermal conductance noise in a bolometer with heat capacity C and thermal conductance G between itself and the heat sink. The photon noise is incorporated through the thermal conductance term. The two terms in the parenthesis represent the voltage fluctuations due Johnson noise in a resistance R and the 1/f excess noise under a bias voltage V_b respectively with k_m being a material and processing dependent 1/f noise parameter. The quantities f_1 and f_2 represent the upper and lower cutoff frequencies of the measurement with the bandwidth given by $\Delta f = f_2 - f_1$ and \mathcal{R} is the bolometer responsivity given by $\mathcal{R} = \alpha V_b / G$. This equation neglects non-equilibrium and electrothermal effects.

For calculating the NEP, the absorbers described in Table 3 are suspended from the heat sink by 10 nm thick Al_2O_3 support legs with electrical contact provided through 20 nm thick NiFe alloy metallization. The support legs are 500 μm long supporting an absorber that is 100 μm square. This choice of materials and geometry ensures a very low support thermal conductance and is just one of the several possibilities. Since we found no published data for the 1/f noise parameter for doped Ge and PbSe, we have used the published values for Vanadium Oxide, a commonly used bolometer material, for the electrical noise calculations [67]. A comprehensive noise analysis is given in the second half of Table 3.

It can be seen from the numbers given in Table 3 that the peak detectivity of these devices is higher than the $1.4 \times 10^{10} \text{ cmHz}^{1/2}/\text{W}$ (for a 4π field of view) blackbody photon noise limit even under real world conditions. The presence of other noise sources reduces the detectivity from that of a purely photon noise limited detector. The time constants of the devices are easily compatible with probable applications in gas sensing and astronomy.

REFERENCES

- [1] R. Kuchibhotla, A. Srinivasan, J. C. Campbell, C. Lei, D. G. Deppe, Y. S. He, and B. Streetman, "Low-voltage high-gain resonant-cavity avalanche photodiode," *IEEE Photon. Technol. Lett.*, 3, 354 (1991).
- [2] K. Kishino, S. Unlu, J.-I. Chyi, J. Reed, L. Arsenault, and H. Mo, "Resonant cavity-enhanced (RCE) photodetectors," *IEEE J. Quantum Electron.*, 27, 2025 (1991).
- [3] E. C. Vail, M. S. Wu, G. S. Li, W. Yuen, and C. J. Chang-Hasnain, "A Novel Widely Tunable Detector with Wavelength Tracking," Postdeadline Paper, *Proceedings of Optical Fiber Communications Conference (OFC)*, Feb./26-Mar./3, San Diego, California (1995), pp18-2
- [4] M. C. Larson, B. Pezeshki, and J. S. Harris, "Vertical coupled-cavity microinterferometer on GaAs with deformable-membrane top mirror", *IEEE Photon. Technol. Lett.*, 7, 382 (1995).
- [5] J. Peerlings, A. Dehe, A. Vogt, M. Tilsch, C. Hebel, Langenham F, P. Meissner, H. L. Hartnagel, "Long resonator micromachined tunable GaAs-AlAs Fabry-Perot filter," *IEEE Photon. Technol. Lett.*, 9, 1235 (1997).
- [6] S. Irmer, J. Daleiden, V. Rangelov, C. Prott, F. Romer, M. Strassner, A. Tarraf, H. Hillmer, "Ultralow biased widely continuously tunable Fabry-Perot filter," *IEEE Photon. Technol. Lett.*, 15, 434 (2003).
- [7] D. Rossberg, "Silicon micromachined infrared sensor with tunable wavelength selectivity for application in infrared spectroscopy", *Sensors and Actuators A: Physical*, 47, 413 (1995).
- [8] H. Alause, F. Grasdepot, J. P. Malzac, W. Knap and J. Hermann, "Micromachined optical tunable filter for domestic gas sensors", *Sensors and Actuators B: Chemical*, 43, 18 (1997).
- [9] Mitsunori Saito and Hideki Furukawa, "Infrared tunable filter by the use of electrostatic force", *Appl. Phys. Lett.* 79, 4283 (2001).
- [10] JT., Daly, W. A. Bodkin, W. J. Schneller, R. B. Kerr, J. Noto, R. Haren, M. T. Eismann, B. K. Karch, "Tunable narrow-band filter for LWIR hyperspectral imaging", *Proceedings of SPIE Vol 3948 Photodetectors: Materials and Devices V*, 1/26-28/00, San Jose, California (2000), pp. 104-115.
- [11] S.-W. Han and D. P. Neikirk, "Design of infrared wavelength-selective microbolometers using planar multimode detectors," *Proceedings of the SPIE Vol. 5836 Smart Sensors, Actuators, and MEMS II, Microtechnologies for the New Millennium 2005*, 05/9-11/05, Seville, Spain (2005), pp. 549-557.
- [12] Vladimir N. Leonov and Donald P. Butler, "Two-color thermal detector with thermal chopping for infrared focal-plane arrays", *Applied Optics*, 40, 2601, (2001).
- [13] Y. Wang, B. Potter, M. Sutton, R. Supino and J. Talghader, "Step-wise Tunable Microbolometer Long-wavelength Infrared Filter", *Technical digest of the 13th International Conference on Solid-State Sensors, Actuators and Microsystems*, 6/5-9/05, Seoul, Korea (2005), pp.1006-1009.

- [14] W. B. Song, M. Sutton, and J. J. Talghader, "Thermal contact conductance of actuated interfaces", *Appl. Phys. Lett.* 81, 1216 (2002).
- [15] R. A. Wood, "Monolithic silicon microbolometer arrays," in *Uncooled Infrared Imaging Systems and Arrays*, New York Academic, (1997), *Semiconductors and Semimetals*, 47, ch. 3, pp. 43-121.
- [16] H. A. Macleod, Thin Film Optical filters. 3rd ed. *Inst of Physics Pub Inc*, (2001).
- [17] E. Palik, Handbook of optical constants. *Academic Press*, (1998).
- [18] K. E. Petersen, "Micromechanical membrane switches on silicon," *IBM J. Res. Develop.*, vol.23, no. 4, pp. 376-385, 1979.
- [19] G. M. Rebeiz, *RF MEMS theory, design, and technology*, 1st ed. Hoboken, John Wiley & Sons, 2003.
- [20] P. F. van Kessel, L. J. Hornbeck, R. FE. Meier, and M. R. Douglass, "A MEMS-based projection display," *Proc. IEEE*, vol. 86, pp. 1687-1704, 1998.
- [21] W. B. Song and J. J. Talghader, "Adjustable responsivity for thermal infrared detectors," *App. Phys. Lett.*, vol. 80, pp. 550-552, 2002.
- [22] Y. Wang, B. J. Potter, and J. J. Talghader, "Coupled absorption filters for thermal detectors", *Opt. Lett.*, vol. 31, pp. 1945-1947, 2006.
- [23] T. Niels, S. Tonny, J. Henri, L. Rob, and E. Miko, "Stiction in surface micromachining," *J. Micromech. Microeng.*, vol. 6, pp. 385-397, 1996.
- [24] W. M. Van Spengen, R. Puers, and I. De Wolf, "On the physics of stiction and its impact on the reliability of microstructures," *J. Adhesion Sci. Technol.*, vol. 17, no. 4, pp. 563-582, 2003.
- [25] C. H. Mastrangelo, "Suppression of stiction in MEMS," invited paper, 1999 Spring MRS Meeting, Boston, MA, Dec 1999.
- [26] B. Bhushan "Adhesion and stiction: Mechanisms, measurement techniques, and methods for reduction," *J. Vac. Sci. Technol. B*, vol. 21, pp. 2262-2296, 2003.
- [27] M. R. Houston, R Maboudian, and R. T. Howe, "Ammonium fluoride anti-stiction treatments for polysilicon microstructures", *Proc 8th Int. conf. On Solid-State Sensors and Actuators (Transducer's 95)*, Stockholm, pp. 210-213, 1995.
- [28] S. Chilamakuri and B. Bhushan, "Contact analysis of laser textured disks in magnetic head-disk interface," *Wear* 230, pp. 11-23, 1999.
- [29] R. Gissi and .P Decuzzi, "The effect of shape and size in micro-/nanodimples adhesion," *J. Appl. Phys.* , vol. 98, 014310, 2005.
- [30] F. Kozlowski, N. Lindmair, W. Lang, T. Scheiter, and C. Hierold "A novel method to avoid sticking of surface-micromachined structures," *Sens. and Actuators A*, vol. 54, pp. 659-662, 1996.
- [31] T. A. Chou, H. Bar, J. Heck, Q. Ma, J. B. Melki, Q. Tran, S. Tubul, B. Weinfeld and N. Ziharev, "Billion-cycle ULV electrostatic RF MEMS switch," *Digest of Solid-State Sensors, Actuators, and Microsystems Workshop of 2006 (Hilton Head'06)*, pp.78-81, Hilton Head Island, South Carolina, June 4-8, 2006.
- [32] M.R. Douglass, "Lifetime Estimates and Unique Failure Mechanisms of the Digital Micromirror Device (DMD)", *Proc. 36th Annual Intl. Reliability Physics Symposium*, Reno,

NV, pp. 9-16, 1998.

[33] B. Staple, D. P. Anderson, and L. Muller, U.S. Patent, 6625342, Sep. 23 2003.

[34] R. Maboudian and R.T. Howe, "Stiction reduction processes for surfacemicromachines", *Tribol. lett.*, vol 3, pp.215-221, 1997.

[35] L. M. Phinney and J. W. Rogers, "Pulsed laser repair of adhered surface-micromachined polycrystalline silicon cantilevers," *J. Adhesion Sci. Technol.*, vol. 17, pp. 603-622, 2003.

[36] V. Gupta, R. Snow, M. C. Wu, A. Jain, and J. Tsai, "Recovery of stiction-failed MEMS structures using laser-induced stress waves," *J. Microelectromech Syst.*, vol.13, pp.696-700, 2004.

[37] J.E. Massad, H. Sumali, D. S. Epp, and D. S. Dyck, "Modeling, simulation, and testing of the mechanical dynamics of an RF MEMS switch," in *Proc. Int. conf. MEMS NANO Smart Syst. ICMENS'05*, Banff, Alberta, Canada, Jul. 22-27, pp.237-240, 2005.

[38] D. A. Czaplewski, H. Sumali, J. E. Massad, J. D. Kupperts, I. Reines, W. D. Cowan and C. P. Tigges, "A soft-landing waveform for actuation of a single-pole single-throw Ohmic RF MEMS switch," *J. , Microelectromech Syst.*, vol. 15, pp. 1586-1594, 2006.

[39] H. C. Nathanson, W. E. Newell, R. A. Wickstrom, and J. R. Davis Jr., "The Resonant Gate Transistor," *IEEE Trans. Electron Devices*, ED-14, No. 3, pp. 117-133, 1967.

[40] A. M. Eihab, Y. I. Mohamed, and N. H. Ali, "Characterization of the mechanical behavior of an electrically actuated microbeam," *J. Micromech. Microeng.*, vol. 12, pp. 759-766, 2002.

[41] Alessandro Granaldi and Paolo Decuzzi, "The dynamic response of resistive microswitches: switching time and bouncing," *J. Micromech. Microeng.*, vol. 16, pp. 1108-1115, 2006.

[42] F W Delrio , M P de Boer, J A Knapp, E Jr David Reedy, P J Clews, and M L Dunn, "The role of van der Waals forces in adhesion of micromachined surfaces," *Nat Mater.*, vol. 4, pp. 629-34, 2005.

[43] W. M. Van Spengen, R. Puers, and I de Wolf, "A physical model to predict stiction in MEMS," *J. Micromech. Microeng.*, vol. 12, pp. 702-713, 2002.

[44] J. A. Knapp and M. P. de Boer, "Mechanics of microcantilever beams subject to combined electrostatic and adhesive forces," vol. 11, pp. 754-763, 2002.

[45] J. M. Huang, K. M. Liew, C. H. Wong, S. Rajendran, M. J. Tan, and A. Q. Liu, "Mechanical design and optimization of capacitive micromachined switch," *Sens. and actuators A*, vol. 93, pp. 273-285, 2001.

[46] M. Bao, H. Yang, "Squeeze film air damping in MEMS", *Sens. Actuators A.*, (2007), doi:10.1016/j.sna.2007.01.008

[47] R. C. Jones, "The ultimate sensitivity of radiation detectors," *J. Opt. Soc. Am.*, vol. 37, no. 11, pp. 879–890, November 1947.

[48] P. B. Fellgett, "On the ultimate sensitivity and practical performance of radiation detectors," *J. Opt. Soc. Am.*, vol. 39, no. 11, pp. 970–976, November 1949.

[49] W. B. Lewis, "Fluctuations in streams of thermal radiation," *Proc. Phys. Soc. London*, vol. 59, no. 1, pp. 34–40, January 1947.

[50] P. W. Kruse, *Infrared Phys. Technol.*, vol. 36, p. 869, 1995.

- [51] R. C. Jones, "Detectivity: the reciprocal of noise equivalent input of radiation," *Nature*, vol. 170, pp. 937–938, 1952.
- [52] K. M. van Vliet, "Noise limitations in solid state photodetectors," *Appl. Opt.*, vol. 6, no. 7, pp. 1145–1169, 1967.
- [53] F. J. Low, "Low-temperature germanium bolometer," *J. Opt. Soc. Am.*, vol. 51, no. 11, pp. 1300–1304, 1961.
- [54] E. E. Haller, M. R. Hueschen, and P. L. Richards, "Ge:Ga photoconductors in low infrared backgrounds," *Appl. Phys. Lett.*, vol. 34, no. 8, pp. 495–497, April 1979.
- [55] D. E. Bode, T. H. Johnson, and B. N. McLean, "Lead selenide detectors for intermediate temperature operation," *Appl. Opt.*, vol. 4, no. 3, pp. 327–331, 1965.
- [56] C. T. Elliot, N. T. Gordon, and A. M. White, "Towards backgroundlimited, room-temperature, infrared photon detectors in the 3-13 μ m wavelength range," *Appl. Phys. Lett.*, vol. 74, no. 19, pp. 2881–2883, May 1999.
- [57] E. H. Putley, "Radiation shielding for uncooled detectors," *Infrared Phys.*, vol. 23, pp. 173–179, 1981.
- [58] P. W. Kruse, *Elements of Infrared Technology*. Wiley, 1962.
- [59] R. W. Boyd, "Photon bunching and the photon-noise-limited performance of infrared detectors," *Infrared Phys.*, vol. 22, no. 3, pp. 157 – 162, 1982.
- [60] P. L. Richards, "Bolometers for infrared and millimeter waves," *Journal of Applied Physics*, vol. 76, no. 1, pp. 1–24, 1994.
- [61] K. C. Liddiard, *Infrared Phys.*, vol. 34, pp. 3790–387, 1993.
- [62] P. Yeh, *Optical Waves in Layered Media*. Wiley, 1988.
- [63] F. J. Low and A. R. Hoffman, "The detectivity of cryogenic bolometers," *Appl. Opt.*, vol. 2, no. 6, pp. 649–650, June 1962.
- [64] H. Y. Fan, W. Spitzer, and R. J. Collins, *Phys. Rev*, vol. 101, p. 566, 1956.
- [65] E. D. Palik, *Handbook of Optical Constants of Solids*. Elsevier, 1998.
- [66] D. R. Lide, Ed., *CRC Handbook of Chemistry and Physics*, 89th ed. CRC Press Taylor and Francis, 2009.
- [67] A. Wood, Ch. 3 in P. W. Kruse and D. D. Skatrud, Eds., *Semiconductors and Semimetals – Vol 47*.
- [68] Y. Wang, B. J. Potter, and J. J. Talghader, "Coupled absorption filters for thermal detectors," *Optics Letters*, vol. 31, no. 13, pp. 1945-1947, July 1, 2006.
- [69] Y. Wang and J. J. Talghader, "Minimum energy actuation and bounce-back behavior of microbeams using δ voltage pulses," *IEEE/ASME Journal of Microelectromechanical Systems*, vol. 17, no. 3, June 2008, p 668-77.
- [70] A. S. Gawarikar, R. P. Shea, and J. J. Talghader, "Thermal Detection Beyond the Blackbody Background Fluctuation Noise Limit," submitted to *IEEE Journal of Quantum Electronics*, 2009.